# PFS: Planetary Fourier Spectrometer

V. Formisano[1], F. Angrilli[2], G. Arnold[3], S. Atreya[4], G. Bianchini[2], D. Biondi[1], M.I. Blecka[6], A. Coradini[1], L. Colangeli[7], V. Cottini[1], A. Ekonomov[8], T. Encrenaz[9], F. Esposito[7], C. Fiorenza[1], S. Fonti[5], M. Giuranna[1], D. Grassi[1], V. Gnedykh[8], A. Grigoriev[8], G. Hansen[10], H. Hirsh[9], I. Khatuntsev[8], N. Ignatiev[8,1], A. Jurewicz[6], E. Lellouch[9], J. Lopez Moreno[11], A. Mattana[1], A. Maturilli[1], M. Michalska[6], B. Moshkin[8], F. Nespoli[1], R. Orfei[1], P. Orleanski[6], E. Palomba[7], D. Patsaev[8], G. Piccioni[12], M. Rataj[6], R. Rodrigo[11], J. Rodriguez[11], M. Rossi[1], B. Saggin[13], D. Titov[8] & L. Zasova[8,1]

[1] *Istituto di Fisica dello Spazio Interplanetario INAF-IFSI, Via del Fosso del Cavaliere 100, I-00133 Roma, Italy*
*Email: formisan@nike.ifsi.rm.cnr.it*
[2] *Universita' di Padova, CISAS, Via Venezia 1, I-35131 Padova, Italy*
[3] *German Aerospace Center (DLR), Optical Information System, Rutherfordstr. 2, D-12489 Berlin, Germany*
[4] *The University of Michigan, Dept. of Atmospheric, Oceanic and Space Sciences, Ann Arbor, MI 48109-2143, USA*
[5] *Universita' degli Studi di Lecce, Dipartimento di Fisica, Via Arnesano, I-73100 Lecce, Italy.*
[6] *Space Research Centre of Polish Academy of Sciences (SRC PAS), Bartycka 18A, 00716 Warsaw, Poland*
[7] *Osservatorio Astronomico di Capodimonte (INAF-OAC), Via Moiariello 16, I-80131 Napoli, Italy*
[8] *Space Research Institute of Russian Academy of Sciences (IKI), Profsojuznaja 84/32, 117997 Moscow, Russia*
[9] *Laboratoire d'Etudes Spatiales et d'Instrumentation en Astrophysique (LESIA), Observatoire de Paris, 5 Place Janssen, F-92195 Meudon, France*
[10] *Planetary Science Institute, Pacific Northwest Division, Dept. of Earth and Space Science, Seattle, WA 98195-1310, USA*
[11] *Instituto de Astrofisica de Andalusia CSIC, POB 3004, E-18080 Granada, Spain*
[12] *Istituto Astrofisica Spaziale INAF-IASF, Via Fosso del Cavaliere 100, I-00133 Roma, Italy*
[13] *Politecnico di Milano, Facoltà di Ing. Meccanica di Lecco, Corso Matteotti 3, I-23900 Lecco, Italy*

**This chapter reviews the first year of results from the Planetary Fourier Spectrometer (PFS) of Mars Express. An average global spectrum ranging from 200 $cm^{-1}$ to 8200 $cm^{-1}$ is compared with the martian spectrum from the Short Wavelength Spectrometer of the Infrared Space Observatory (ISO), and with the global synthetic spectrum computed using only the gases $CO_2$, CO and $H_2O$. PFS is able to measure the vertical temperature–pressure profile in the atmosphere and the temperature of the soil simultaneously with the dust and water-ice opacity. The short-wavelength channel shows the major $CO_2$ bands at 4.3 μm and 2.7 μm. The bottom of the first band shows very clearly the non-local thermodynamic equilibrium emission of the high atmospheric $CO_2$ gas, while the limb measurements show CO emission. All the isotopic $CO_2$ molecules appear to be emitting at the same radiance level, implying strong energy pumping from the most abundant to the less abundant molecules. In one of the first passes over Olympus Mons, the temperature field shows abnormal adiabatic cooling in the atmosphere above the mountain, while the soil temperature of the volcano is higher than the latitudinal profile expectation because of illumination from the Sun. The descending branch of the Hadley cell circulation is studied in detail, with its adiabatic heating and formation of water-ice clouds. Of the many unidentified lines observed, a few have been studied and the presence of methane (10 ppbv), HF (200 ppbv) and HBr (150 ppbv) is reported here. PFS has allowed the study of the composition of the permanent south polar cap: an intimate**

**mixture model of mostly $CO_2$ ice, ppm of water ice and some dust fits the data very well. Almost pure water-ice and $CO_2$-ice spectra have been observed in specific locations. Finally, many solar lines are being observed; a few are being studied and compared with ISO observations and the solar spectrum assembled for PFS. In certain spectral regions, Mars looks like a Lambertian screen, reflecting an almost unperturbed solar spectrum.**

# 1. Introduction

Following arrival in orbit around Mars on 25 December 2003, the Planetary Fourier Spectrometer (PFS) on Mars Express was activated on 10 January 2004. Routine operations for each orbit cover calibration, observation and then calibration again. The observed spectra, although showing evidence of the craft's micro-vibrations, immediately gave the flavour of a dataset extremely rich in information. The team could immediately arrange for a number of publications describing the experiment, its performance and its scientific validation, in particular, Formisano et al. (2005a) for the experiment description and Giuranna et al. (2005a, b) for the calibrations. The method of retrieving the atmosphere's temperature–pressure vertical profile is described in Grassi et al. (2005a); the method of fast synthetic spectra computation is presented in Ignatiev et al. (2005). A number of scientific results were also obtained, and they were highly appropriate for scientific validation of the experiment and of the data obtained. This chapter reviews some of the presented results (Formisano et al., 2005b; Grassi et al., 2005b; Zasova et al., 2005) and adds unpublished data, with the aim of bringing to the attention of the scientific community the characteristics of PFS data and stressing the importance of the information in the data.

### 1.1 Experiment Characteristics and Present Global Coverage

PFS is an IR spectrometer optimised for atmospheric studies. It has a short-wavelength (SW) channel covering the spectral range 1700–8200 $cm^{-1}$ (1.2–5.5 μm), and a long-wavelength (LW) channel covering 250–1700 $cm^{-1}$ (5.5–45 μm). Both channels have a uniform spectral resolution of 1.3 $cm^{-1}$, while the sampling is every 1 $cm^{-1}$. The instrument Field of View (FOV) is about 1.6° Full Width Half Maximum (FWHM) for SW, and 2.8° FWHM for LW, which corresponds to spatial resolutions of 7 km and 12 km, respectively, when Mars is observed from a height of 250 km.

In comparison with the classical Michelson interferometer, the design (Formisano et al., 2005a) is highly robust against slight misalignments in harsh environments. Mechanical vibrations from the spacecraft affect the main radiation beam and the reference channels used to drive the experiment in the same way, so that meaningful measurements can still be taken. Double-sided interferograms are taken because they are relatively insensitive to phase errors – an important point for computing the martian spectrum.

Figure 1 shows the coverage of the planet achieved by April 2005, after more than a year of operations. By then, more than 190 000 measurements had been collected, each consisting of an LW interferogram and an SW interferogram. The coverage of the planet is very good; the extended mission aims to achieve four times this coverage. Figure 2 shows the north polar region coverage either illuminated (Fig. 2a) or not (Fig. 2b); it is evident that the coverage of the northern polar cap has been rather good when illuminated, but less so when not illuminated. Figure 3 presents the equivalent coverage of the southern polar cap. Owing to the season, the team has good coverage of the cap on the night side and limited coverage with solar illumination.

Figure 4 shows the latitude–local time coverage, an important aspect because the study of diurnal variation of several parameters is an important scientific objective. The local time coverage is rather good, but it is biased by season, i.e. season and local time are strongly linked. So far, there are no measurements of the equatorial region at midnight. It will be necessary to use the pointing mirror to fill this gap because the pericentre of the orbit, although it travels over all latitudes in time, will never reach the midnight regions at the equator.

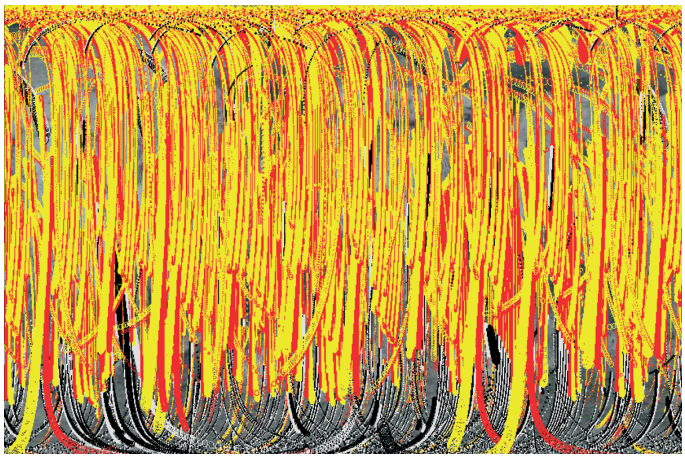

**Fig. 1. PFS coverage of Mars up to 18 April 2005, after more than a year of operations. The vertical axis shows latitude, the horizontal axis shows longitude. The footprint of the LW channel is in red (if with solar illumination), while the SW footprint is in yellow. The grey footprints indicate no solar illumination.**

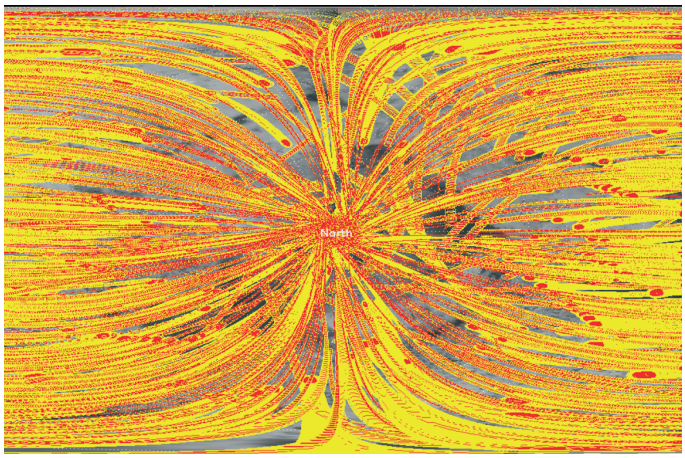


**Fig. 2. (a) North polar cap coverage with illuminated conditions. The north pole is at the centre.**

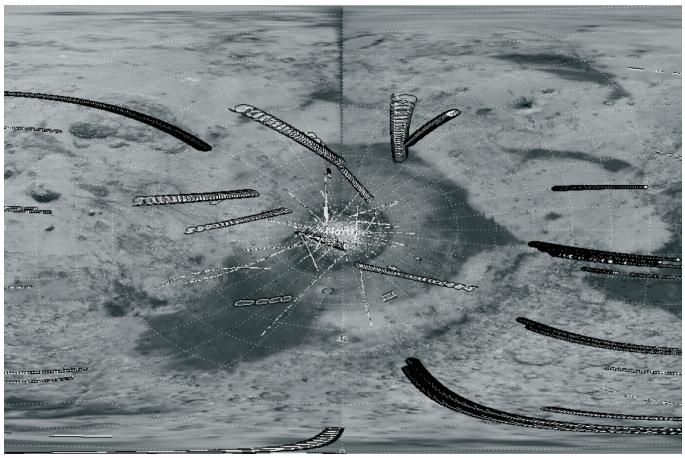

**Fig. 2. (b) North polar cap coverage with unilluminated conditions. The north pole is at the centre. LW = black; SW = white.**

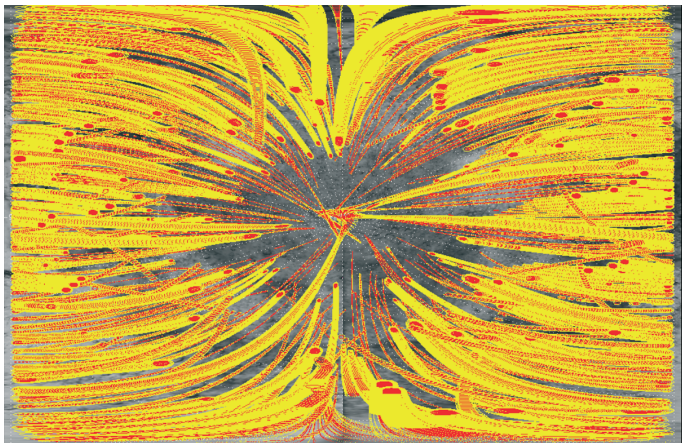

**Fig. 3. (a) South polar cap coverage to 11 April 2005 with illuminated conditions. The south pole is at the centre.**

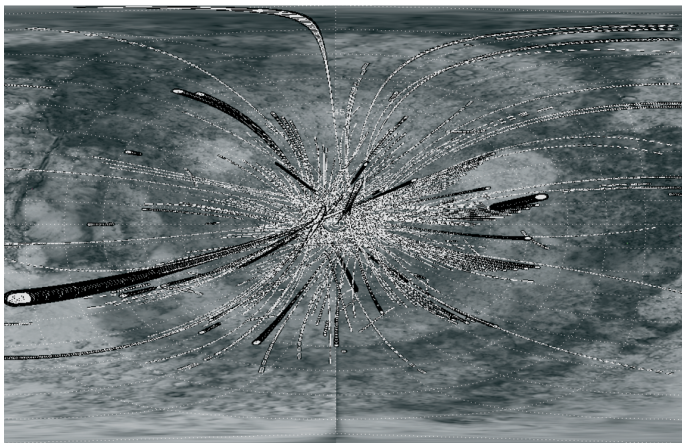

**Fig. 3. (b) South polar cap coverage with unilluminated conditions. The south pole is at the centre. LW = black; SW = white.**

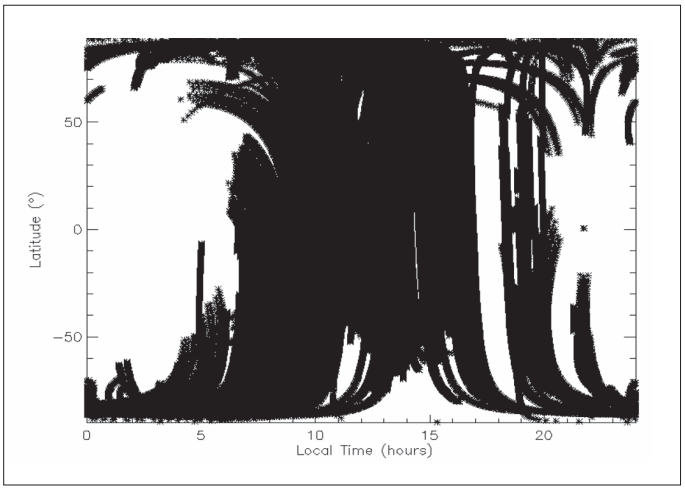


**Fig. 4. Latitude-local time coverage of PFS observations for orbits 10–1610, covering more than a year.**

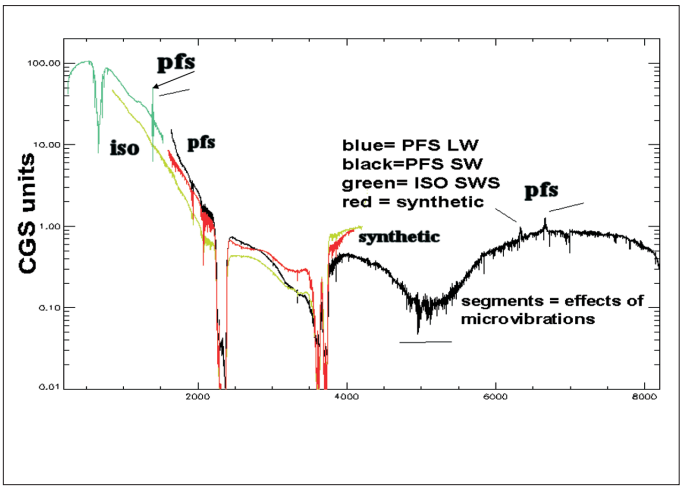


**Fig. 5. PFS LW channel (green curve) and SW channel (black curve) compared with the ISO SWS spectrum of Mars (yellow curve) and a synthetic spectrum (red curve, computed using radiative transfer modelling of the atmosphere). Disturbance peaks above 6000 cm$^{-1}$ disappeared after switching off the SW channel laser diode.**

## 2. An Average PFS Spectrum

In order to validate the PFS data scientifically, an average spectrum was computed for comparison with Infrared Space Observatory (ISO) Short-wavelength Spectrometer (SWS) measurements of Mars. The details of how this average was computed are given in Formisano et al. (2005b). The 16 orbits considered were distributed over all longitudes for latitudes between –50° and +45°. In local time, the data were between 1200 LT and 1400 LT. Data selection was done by choosing high signal-to-noise ratio (SNR) spectra from uncalibrated data. The following also compares PFS results with a synthetic spectrum, computed with radiative transfer modelling of the martian atmosphere, and line-by-line computation. The computed spectra were with only the gases $CO_2$, $H_2O$ and CO or added aerosols (dust and water-ice particles). The global spectra of both PFS and ISO are shown in Fig. 5. PFS radiance is larger than that from ISO from 1600 cm$^{-1}$ up to 3200 cm$^{-1}$, while ISO's is larger above 3750 cm$^{-1}$. The first is understood in terms of higher ground temperature of Mars for PFS observations; the second is explained by the higher albedo for the ISO observations. The average soil temperature for the PFS average observations was 275.5K. Indeed, a Planckian curve of 275.5K fits the LW channel spectrum rather well. Note that the Planckian curve also fits the measured spectrum well between 1750 cm$^{-1}$ and 2350 cm$^{-1}$. Above that last value, the solar radiance dominates. The ISO ground temperature was 240K (Formisano et al., 2005b).

The larger ISO radiance above 3750 cm$^{-1}$ arises from the higher soil albedo and lower dust opacity with respect to the PFS average. Indeed, the sub-solar region for ISO observation was the Tharsis region, where there is higher albedo *per se*, and also higher elevation, which necessarily means lower dust opacity. The different dust/water-ice content in the atmosphere between the two observations is also revealed by two other features: the radiance inside the $CO_2$ band at 2.7 μm, which is clearly higher in the PFS observation, and a band observed between 3100 cm$^{-1}$ and 3500 cm$^{-1}$ due to water ice. The possibility of using the radiance inside the two large $CO_2$ bands for measuring the atmospheric dust content was proposed by Titov et al (2000). The details of the two major $CO_2$ bands are discussed later in this chapter.

Figure 5 also shows a comparison of the PFS average spectrum with a synthetic spectrum computed for a soil temperature of 275.5K and albedo 0.2 constant over the range. It shows that between 1600 cm$^{-1}$ and 1750 cm$^{-1}$ the observed radiance tends

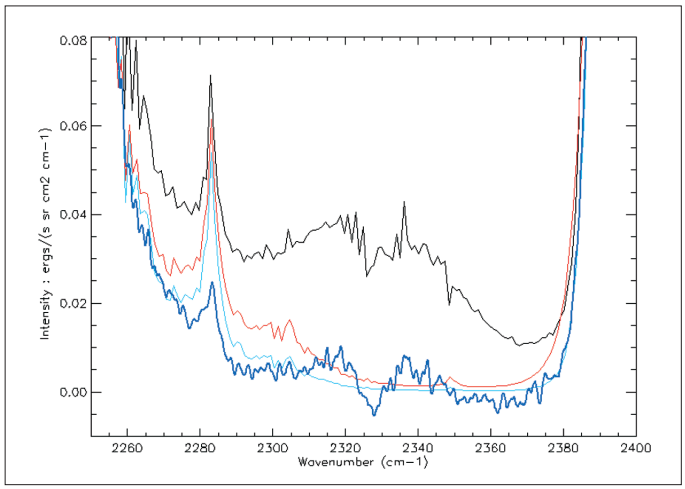


**Fig. 6. (a) The bottom of the $CO_2$ band at 4.3 µm. ISO SWS is the dark blue line, PFS the black line, light blue is synthetic with no dust, red is synthetic with dust in the atmosphere.**

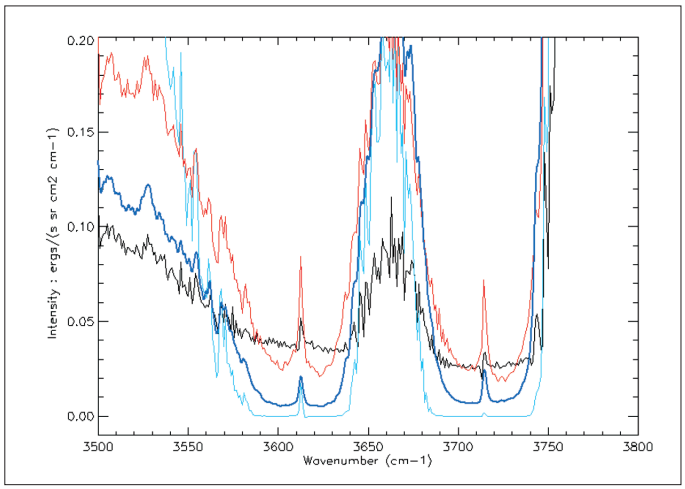


**Fig. 6. (b) $CO_2$ band at 2.7 µm for the same four spectra as in (a).**

to be larger than the computed one, owing to the very low responsivity of the PFS SW channel in this range. The experiment was not designed to detect radiance in this range, so any capability below 2000 $cm^{-1}$ is a bonus. *A posterior* this is considered a very positive result because mechanical vibrations destroy this same wavenumber range in the LW channel. The radiance, however, below 1750 $cm^{-1}$ has a much larger error bar.

The synthetic spectrum shows that both the main $CO_2$ bands are much deeper than was observed; the amount of dust included was not enough. Non-local thermodynamic equilibrium (non-LTE) effects, on the other hand, can produce emission from the upper atmosphere, observed by PFS in the 2200–2400 $cm^{-1}$ band (Lopez-Valverde et al., 2005).

There is a large difference between the synthetic and measured spectra between 3000 $cm^{-1}$ and 3500 $cm^{-1}$. In principle, it could be due either to soil features or aerosols. Both effects are probably present, but certainly water-ice clouds are important and perhaps dominant, as can be deduced from several other synthetic spectra (not shown here for brevity) computed by the team for different ice opacities.

The radiance profile inside the 4.3 µm $CO_2$ band is given in Fig. 6(a). The ISO radiance is negative at the centre, meaning that the ISO spectrum had a zero radiance level problem. The ISO data are shown smoothed over 11 points to reduce the noise, but the effect on spectral resolution is minor. The radiance variation observed in the ISO spectrum was interpreted (Lellouch et al., 2000) as due to non-LTE effects in the atmosphere. In order to have the ISO minimum above the zero level, a radiance value of 0.007 erg/(s sr $cm^2$ $cm^{-1}$) must be added. The minimum radiance in all four curves is observed at 2370 $cm^{-1}$. The synthetic spectrum (no dust) is equal to zero there, ISO has –0.005 erg/(s sr $cm^2$ $cm^{-1}$), and PFS has 0.01 erg/(s sr $cm^2$ $cm^{-1}$). Adding the zero offset, the difference between ISO and PFS becomes 0.008 erg/(s sr $cm^2$ $cm^{-1}$). The inclusion of dust in the computation of the synthetic spectrum adds a level in the bottom of the band, but PFS has certainly more dust than in the computation. Note that non-LTE effects seem to generate up to 0.017 erg/(s sr $cm^2$ $cm^{-1}$); the difference ISO – PFS at the band minimum is half this value and can be due either to stronger non-LTE effects (all PFS data are at 13:00–14:00 local time, the maximum of the daily thermal variation) or to dust contributions.

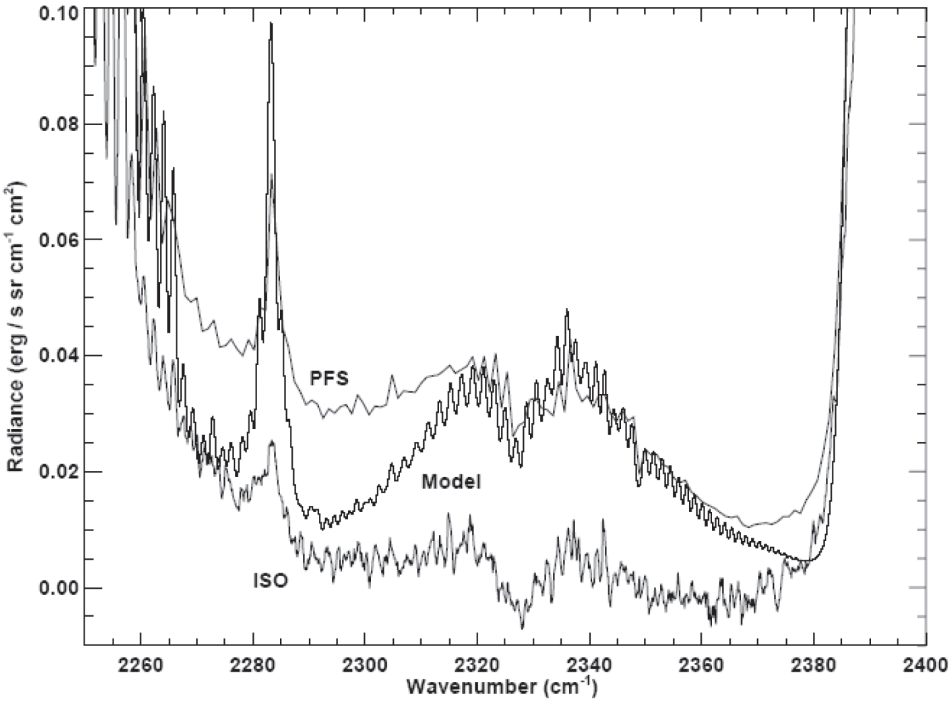


**Fig. 7. Emitted radiance, computed from a non-LTE model, fitting the observed PFS radiance inside the 4.3 μm band.**

The non-LTE PFS observations have been fitted with a theoretical numerical result by Lopez-Valverde et al. (2005). They have shown that it is the $CO_2$ second hot band that produces the observed features (the R- and P-branches of the second hot band are the two structures observed on the two sides of the 2328 cm$^{-1}$ band). In order to explain the observed radiance, however, they have shown that a good fit could only be obtained after combining a large increase in the V–V relaxation with single scattering in the second hot bands. The resulting fit is shown in Fig. 7, where the PFS and ISO SWS measurements are again shown, together with the radiance resulting from modelling.

The radiance inside the 2.7 μm band (Fig. 6b) is a measure of the aerosol content in the atmosphere. In the PFS data the radiances in the two $CO_2$ bands (3580–3635 cm$^{-1}$) and (3690–3740 cm$^{-1}$) clearly differ. This could indicate spectral properties of the dust grains, as suggested by Fedorova et al. (2002).

In the case of ISO, dust opacity was evaluated to be 0.2, while using the Fig. 2 of Titov et al. (2000) for PFS produces an average value of 0.5, in agreement with other findings from PFS data. PFS average dust opacity at 1100 cm$^{-1}$ in this period was 0.3, which indicates a ratio between 2.7 μm and 9 μm of 1.66, in agreement with the ratio of 2.5, usually quoted, between visible and thermal-IR (Clancy et al., 1995).

The behaviour of the Noise Equivalent Radiance (NER) for the two channels is such that (Giuranna et al., 2005a,b) the SNR for the $CO_2$ 15 μm band is larger than 150 for a single measurement, and that the radiation inside the 4.3–2.7 μm band is measured with an SNR larger than 100 (thanks to the averaging of 1680 spectra).

### 2.1 Non-LTE Emissions at the Limb

In all nadir observations, the bottom of the 4.3 μm band shows the emission modelled in Fig. 7. The complete picture of the non-LTE emission, however, is obtained with PFS limb measurements. Figure 8 shows data from one such orbit (orbit 1234), when the PFS FOV was always above 80 km altitude. Most of the non-LTE emission is normally masked by the thermal emission of the soil and the reflected solar radiation. Only the limb measurements show all the details of the emission. Figure 8 includes CO observed in emission; it can be shown that it is the first hot band of CO. $CO_2$

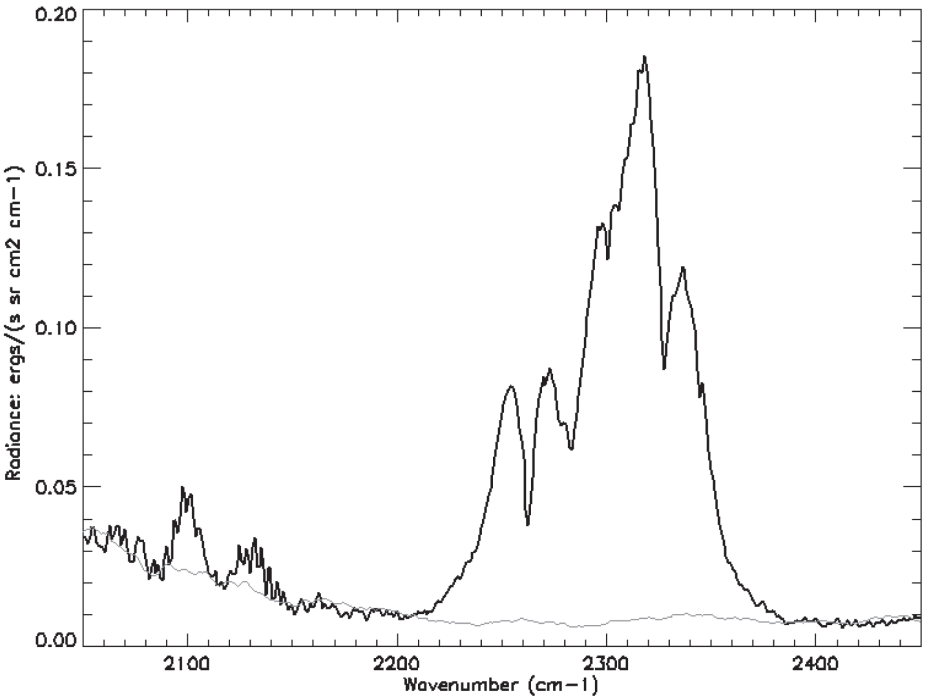


**Fig. 8. Limb observation of non-LTE emission from CO and $CO_2$. The grey curve is the deep-space zero-radiance level.**

emission shows a structure that, when studied in detail (Formisano et al., 2005c), can be interpreted as due to the isotopic molecules of $CO_2$. The 636, 626 and 628 isotopic molecules are emitting at almost the same intensity, which implies a very strong pumping of energy from the main isotope 626 to the others via collisions. It can be shown that the 626 and 636 isotopic molecules are emitting the second hot band, while the 628 is emitting the third.

## 3. Results from the LW Channel

The LW channel covers the thermal region 250–1700 $cm^{-1}$. Spectral resolution is of the order of 2 $cm^{-1}$ for apodised spectra, sampled with a 1 $cm^{-1}$ step. The instantaneous FOV of the channel has a diameter of 12.2 km at the nominal height of the 250 km pericentre. A complete description of the instrument and its radiometric performances can be found in Formisano et al. (2005a) and Giuranna et al. (2005a).

The PFS spectra can be analysed individually using the methods and tools presented by Grassi et al. (2005a). The algorithm computes the effects of multiple scattering by atmospheric aerosols. Retrieval of atmospheric fields is limited to surface temperature, air temperature vs. altitude (up to 45–50 km), dust and water-ice integrated contents. Dust concentration is assumed to scale exponentially with altitude, according a decay height of 10 km. Results presented in this work were achieved by assuming that the water-ice particle concentration vs. altitude is described by an exponential shape with a 10 km decay height.

An important problematic aspect of the temperature retrieval method arises from the assumptions made to define the value of $P_{surf}$ (atmospheric pressure at the surface), to be adopted in the definition of a suitable temperature vs. pressure grid during evaluation of synthetic spectra. Values projected by models were used integrated with Mars Global Surveyor's Mars Orbiter Laser Altimeter (MOLA) data (Smith et al., 2003). In the future, the SW channel data will be used to obtain the team's own measured $P_{surf}$. The non-saturated $CO_2$ bands at solar wavelengths (e.g. 5000, 6350 and 6950 $cm^{-1}$) allow the retrieval of the integrated content of $CO_2$ (i.e. $P_{surf}$), with an error of the order 0.25 mbar or lower.

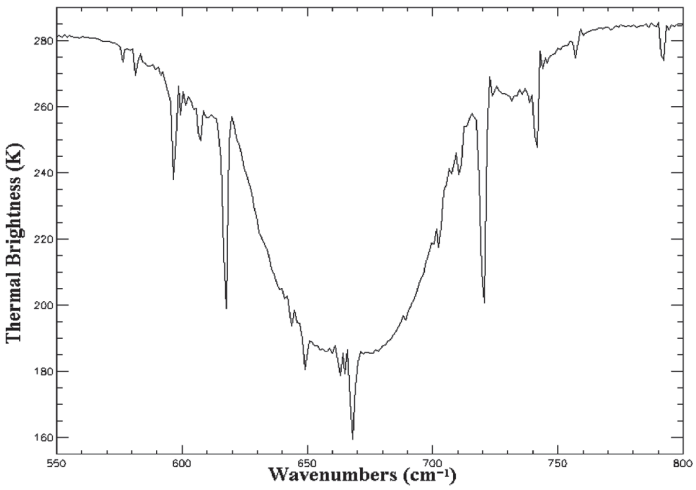


Fig. 9. (a) Enlargement of the 15 µm $CO_2$ band, unapodised spectrum. Note the many Q-branches and their isotopic satellites.

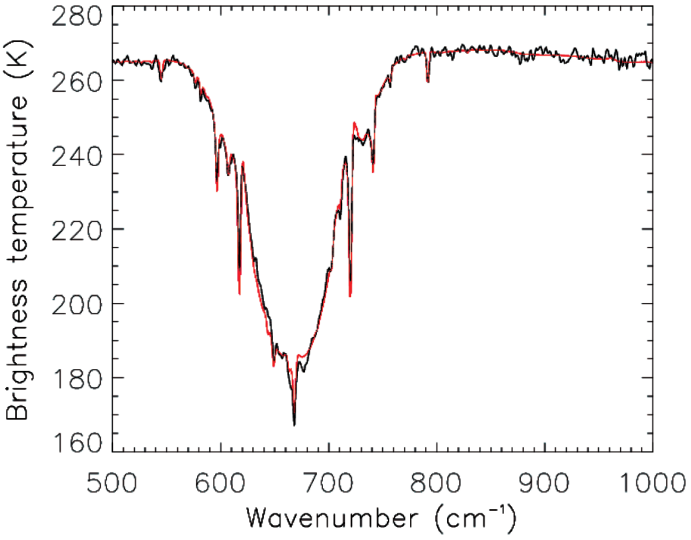


Fig. 9. (b) The 15 µm $CO_2$ band fitted with the synthetic spectrum computed from the temperature profile-retrieval procedure.

Fig. 10. The thermal field from orbit 37, covering Olympus Mons.

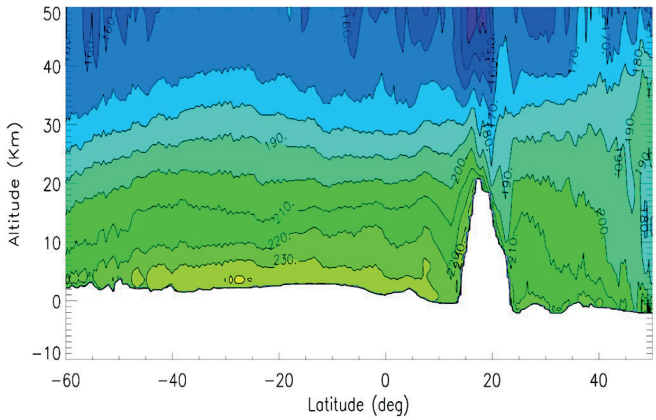


### 3.1 Atmospheric Temperatures

Figure 9 presents the $CO_2$ 15 µm band. The bottom of the band clearly shows several Q-branches, the main one being due to $O^{16}C^{12}O^{16}$ (usually known as the 626 isotopic molecule); the others are due to all the $CO_2$ isotopic molecules. On the left of the 626 large Q-branches at 668 $cm^{-1}$ there are the well-resolved Q-branches for the isotopic molecules $O^{16}C^{12}O^{18}$ at 663 $cm^{-1}$ and $O^{16}C^{12}O^{17}$ at 665 $cm^{-1}$. This will allow the abundances of these isotopic molecules to be evaluated. Figure 9(b) shows a single LW spectrum from PFS fitted with the synthetic spectrum resulting from the temperature profile retrieval process. Putting together all the temperature profiles from one orbit (the spacecraft trajectory is essentially always north–south along a meridian) provides the atmospheric temperature fields. Figure 10 shows the retrieved air thermal field on orbit 37, passing over Olympus Mons. The general behaviour is similar, in the regions far from the mountainous relief, to that of the Global Circulation Model (GCM) (Forget et al., 1999). When comparing the details, however, it is found that the thermal field measured by PFS is somewhat warmer (10–15K) than predicted by the European Mars Circulation Dataset (EMCD) for the Mars Global Surveyor dust scenario. This discrepancy is probably due to the different dust load in the atmosphere. Adopting a value for dust opacity ratio of $\tau_{vis}/\tau_{IR} \approx 2$, PFS measurements exceed

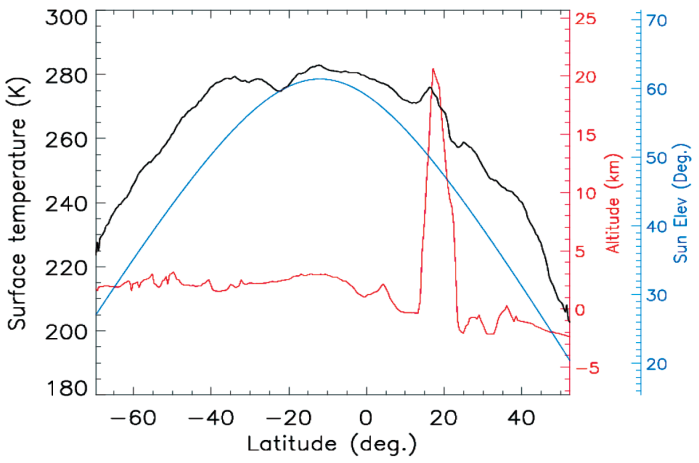


**Fig. 11. Soil temperature, Sun elevation and altimetry above Olympus Mons.**

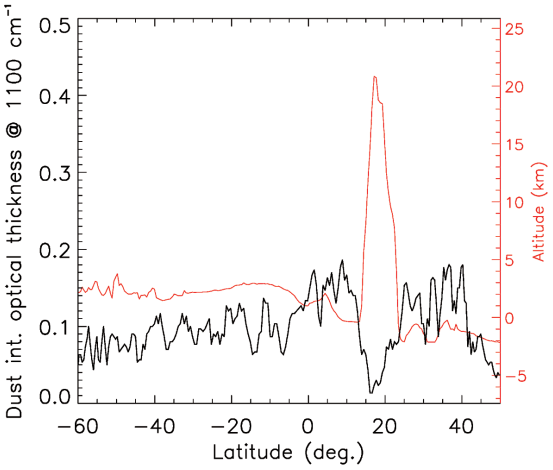


**Fig. 12. Altimetry and dust content over Olympus Mons.**

model assumptions by a factor ~2–2.5. The capacity of martian aerosols to raise the average air temperature fields has been well established since the Mariner-9 IRIS observations (Conrath, 1975) and was confirmed by Thermal Emission Spectrometer measurements from Mars Global Surveyor (Smith et al., 2000). The temperature fields retrieved by PFS in the first ~5 km above the surface should be viewed with caution because the error bar could be larger there.

The most complex situation is observed in the region around Olympus Mons. There, EMCD provides a poor reference because the model does not currently include meso-scale phenomena.

A useful comparison can be made between the air temperatures retrieved close to and far from the dome at a given altitude:

— the most interesting structure is represented by the air temperature minima centred around 45 km altitude and 20°N latitude. The lower boundary of the cold region lies at ~35–40 km altitude, where PFS data can still provide some useful information, even if just from the tails of weighing functions. No similar structure is visible in the thermal field expected from the model, used as *a priori* during retrieval. Consequently, the minima can be taken as real with confidence.
— the air on the lowest atmospheric levels on the southern flank of the dome, where there is more direct sunlight owing to the local topography and the Sun zenith angle, shows values up to 220K, even when the less reliable altitude range closer to surface is neglected. Values of about 20K lower are observed on the northern flank when the same altitudes above the surface are taken into account. These fields are related to moderate vertical thermal gradients, of the order 1.5–2K/km, in comparison with an indicative adiabatic thermal gradient for Mars of around 4.5K/km (Zurek et al., 1992). Higher thermal gradients are measured only in the lowest levels of atmosphere.
— a heating branch is observed around 16.5°N, extending up to 40–45 km. This structure strictly correlates with the topographical profile; the vertical temperature gradient is fairly constant over the volcano's shield.
— air temperatures at the boundaries of the volcano shield present local minima from the surface up to 30 km. Cooling branches seem to be present at 12°N and 24°N.

All the structures identified above indicate the need for a meso-scale modelling of the atmosphere, with possible consequences on the global scale. In other words,

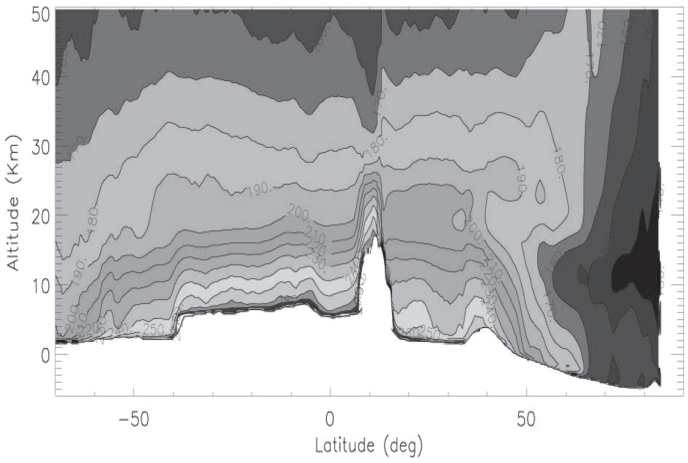


**Fig. 13. Temperature field (isolines) vs. altitude and latitude along orbit 68, which passes through Tharsis (ϕ < 40°S), Ascraeus Mons (10°N) and the edge of Alba Patera (40°N). Temperatures are retrieved after averaging over four single spectra, except for Ascraeus Mons (averaged over two spectra) and the northern polar region (10 spectra).**

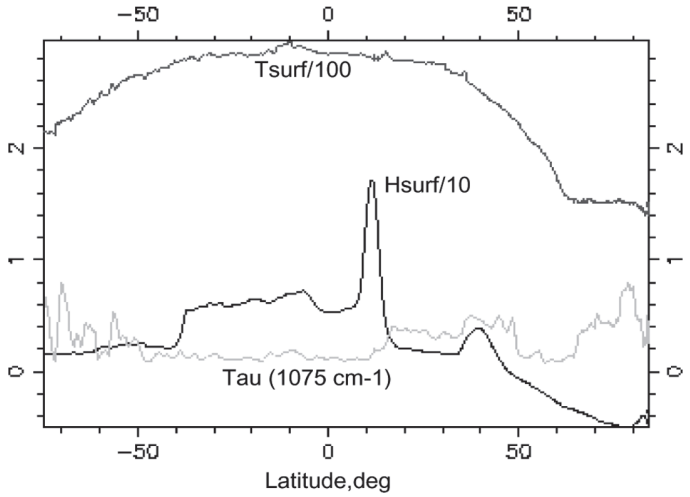


**Fig. 14. Surface temperature ($T_{surf}$ divided by 100), surface altitude ($H_{surf}$ divided by 10) and aerosol opacity (Tau) along orbit 68.**

observations over local altimetry features are important because they may have consequences for the global planetary circulation.

### 3.2 Surface Temperatures

Figure 11 shows the surface temperature trend measured by PFS during a pass over Olympus Mons. The Sun elevation above the surface of the reference geoid and topographic profile are also reported for comparison. The general trend driven by solar illumination dependence on latitude has a remarkable anomaly above the dome, represented by the high warming of about 10K between 15°N and 21°N. By contrast, the surface temperature measured around 23°S is lower than expected from the large-scale trend. A complete simulation of surface temperatures, including geometrical conditions, surface thermal inertia (taken from, for example, TES measurements, Mellon 2002), digital terrain modelling and aerosol opacity is under development. From a qualitative point of view, surface orientation (the southern flank is more exposed to the Sun) and dust (shielding against incoming solar energy) play major roles in driving the temperature.

### 3.3 Integrated Dust Content

The integrated dust content is presented in Fig. 12 for the passage over Olympus Mons. The effect of different atmosphere thickness owing to dome height is evident, with low dust opacities near the dome's summit. Once an exponential decay of dust concentration with height is assumed, the fit of PFS-retrieved dust content vs. MOLA topography allows a crude estimation of dust scale-height. The retrieved values have a number of error sources (limited statistics, dust content uncertainties, finite size of FOV) that may lead to cumulative effects that are hard to quantify. The results point to a figure for the scale-height of around 10 km, on both the southern (11.9 ± 1.9 km) and northern (9.6 ± 2.7 km) flanks of the volcano. The extrapolated value of integrated dust at zero altitude is also quite symmetric in latitude: 0.16 ± 0.02 for the southern side and 0.19 ± 0.07 for the northern flank.

### 3.4 The Polar Hood

Figure 13 shows the temperature field in latitude–altitude coordinates along orbit 68. It begins at 70°S, passes over Tharsis, Ascreaus Mons, the edge of Alba Patera and the northern polar region.

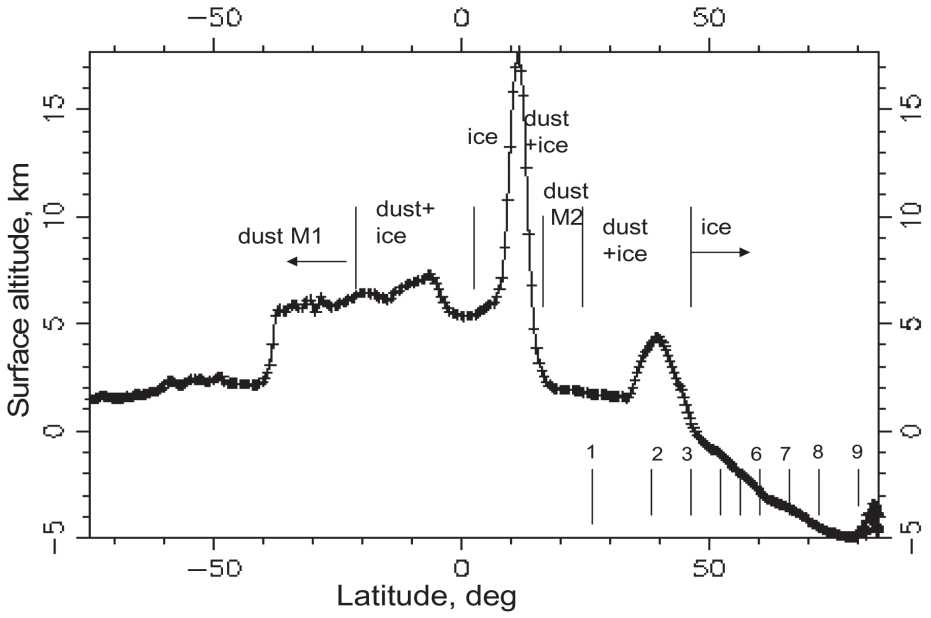


**Fig. 15. Surface altitude along orbit 68. The latitude ranges where the aerosols are water-ice clouds, dust or both are shown. The vertical lines at bottom right show the positions of the spectra in Fig. 17(a,b). The terminator is at about 76°N.**

Temperature profiles were retrieved from the spectra averaged over four individual spectra. They were averaged over two spectra for the case of Ascraeus and over 10 for the northern polar region above 60°N. The low temperature in the northern polar region leads to a low SNR, especially in the short wavelengh part of the 15 μm band. Averaging over 10 spectra increases the effective FOV up to 200 km. Both Ascraeus and Alba Patera have lower altitudes in the plot because the coordinates are also smoothed. The results of the retrieval from individual spectra for parts of the orbit, where the SNR is high enough, are presented in Grassi et al. (2005b).

The maximum of the surface temperature is found in the low southern latitudes, $\phi = 0$–20°S. Another maximum occurs on the southern slope of the volcano near the caldera. It is clearly noticeable in Fig. 13 that the sharpest temperature gradient is observed above the regions with the highest surface temperatures. At latitudes exceeding 60°N, the temperature becomes low enough for $CO_2$ ice to condense. Indeed, the edge of the northern seasonal polar cap is observed around 62°N; it is clearly seen in Fig. 14, where the surface temperature, surface altitude and the dust opacity are presented along orbit 68.

For latitudes above 50°S, opacity changes from 0.1 to 0.8. High values of dust opacity may be caused by a local dust storm. The water-ice clouds appear in the PFS FOV only at southern low latitudes. Up to around 20°S the spectral shape may be explained by the aerosol composed of Toon mode 1 particles with effective radius $r_{eff} = 1.65$ μm. In the southern tropics <20°S above Tharsis, the water-ice aerosol should coexist with the dust (averaged over the PFS FOV). However, at 1075 $cm^{-1}$ the opacity is still defined by dust: the contribution of the ice aerosol is much less significant in this spectral range. A minimum opacity at 1075 $cm^{-1}$ is observed in those latitude ranges where the ice clouds cover most of the FOV. The latitude ranges where the dust, ice and dust+ice clouds are observed are shown in Fig. 15.

Considering orbit 68, below 10 km on the northern flank of the Ascreus volcano the ice clouds are not visible in the spectra and up to 25°N the aerosol is well described by the dust particles of Toon mode 2 size distribution. Further along the orbit, close to Alba Patera, the water-ice aerosols coexist with the dust (in the PFS FOV) up to 48°N. Above 48°N, the polar hood is observed and the shape of the spectrum shows that the ice clouds dominate there. The thermal–IR spectrum is sensitive to the water-ice particle size; the best fit is obtained with ice particles of $r_0 = 4$ μm.

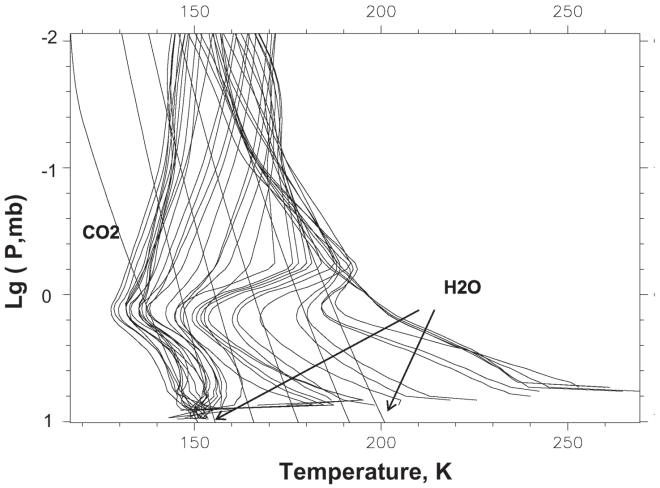


**Fig. 16. Temperature profiles obtained from the spectra on orbit 68 at $\phi > 30°N$; approximately every tenth profile is shown to avoid overlapping). Dashed-dotted lines mark the temperature of the $H_2O$ condensation at 0.1, 1, 10, 100, 200, 300 and 400 ppm, respectively. Dashed lines present the temperatures of the $CO_2$ condensation.**

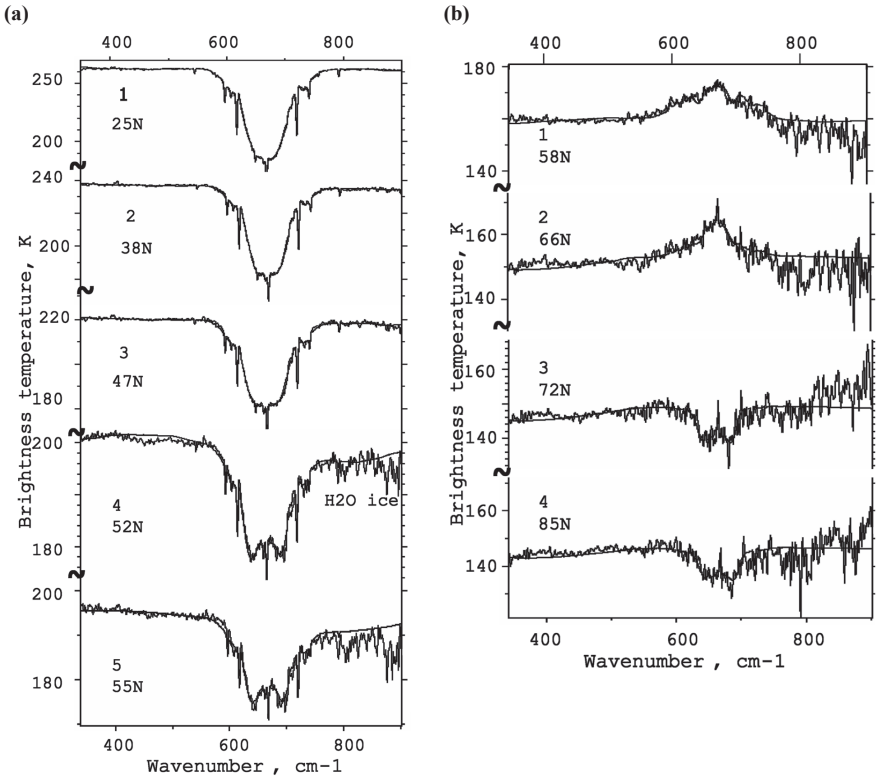


**Fig. 17. (a) Examples of the PFS spectra in the latitude range 30–55°N, together with the synthetic spectra calculated for the retrieved parameters. The variation of the shape in the centre of the 15 μm $CO_2$ band is explained by the different forms of the temperature profiles. The positions of the spectra along the orbit are shown in Fig. 15.**

**Fig. 17. (b) As Fig. 17(a), but for latitudes 60–85°N.**

**Fig. 17. (c, below) Temperature profiles obtained from the spectra in Fig. 17(a). Approximate altitude is given on the vertical axis. Dashed lines show the temperatures of $H_2O$ condensation at 10, 100 and 200 ppm.**

**Fig. 17. (d, below right) As Fig. 17(c), but from the spectra in Fig. 17(b). The dashed line shows the temperature of $CO_2$; the dotted lines show the temperatures of $H_2O$ condensation at 0.1, 1, 10, 100 and 200 ppm.**

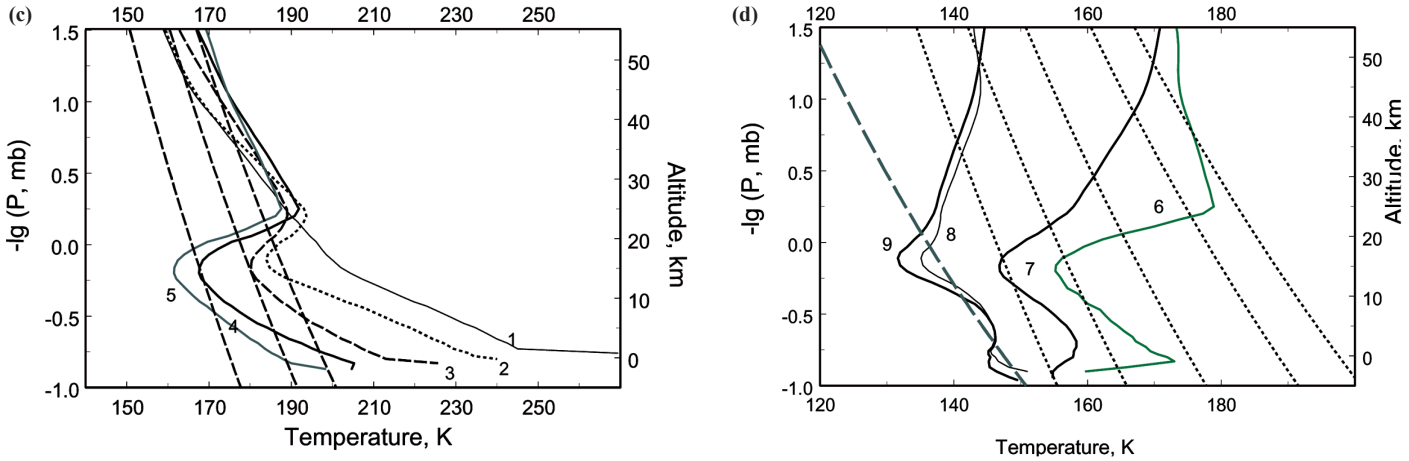

At $\phi > 50°$ the ground temperature is low enough for water-ice to be on the surface. The aerosol is again observed as water-ice clouds. The best fit is obtained for the water-ice aerosol having a mean particle size of $r_0 = 4$ μm. Beyond 62°N, the surface temperature along the orbit drops to 150K. Indeed, the $CO_2$ polar cap begins there.

An elevated inversion in the temperature profiles, with amplitude about 3–5K, appears above Alba Patera (Fig. 14), with minimum near 1.3 mb and maximum around 0.6 mb. The amplitude of inversion increases to the north up to the edge of the $CO_2$ polar cap. The altitude of the temperature maximum also increases. Above the $CO_2$ polar cap, the spectrum at PFS resolution is not sensitive enough to determine the position of the maximum: it demonstrates the monotonic increase of the temperature vs. altitude, above the minimum at around 1 mb.

Figure 16 provides examples of the retrieved temperature profiles (approximately every tenth profile is shown), demonstrating the development of the elevated inversion. A group of temperature profiles without inversion is found at $\phi < 30°$N. From Alba Patera up to the edge of the $CO_2$ polar cap, all temperature profiles reveal a strong elevated inversion. Figure 17(a) gives the spectra together with the synthetic versions for $\phi < 62°$N; the position of each spectrum along the orbit is shown in Fig. 15. Above the seasonal cap, where the surface temperature decreases to $CO_2$ condensation, the shape of the temperature profiles change in such a manner that above the minimum at around 1 mb the atmospheric temperature increases monotonically. The temperature profile near the surface above the $CO_2$ polar cap is not discussed here, because it needs a more careful investigation of the surface composition. This work used the surface emissivity of $CO_2$ frost mixed with dust. However, even a very small amount of water-ice added to the $CO_2$ ice on the surface may change the surface emissivity significantly (Hansen et al., 2005), which in turn may change the ice aerosol opacity in the near-surface layer and influence the near-surface temperature profile. In the polar night the retrieved temperature in some cases is lower than the temperature of the $CO_2$ condensation, which may be caused by low emissivity of $CO_2$ clouds. However, another possibility may be super-saturation, which was identified in the temperature profiles during polar night at both poles by radio occultation measurements from Mars Global Surveyor.

Figure 17(b) shows the spectra above the $CO_2$ polar cap. Spectra 8 and 9 have similar shapes but slightly different brightness temperature; one was obtained near the terminator and the other in polar darkness. Both reveal a low brightness temperature in the 15 μm band and hence a low temperature at the corresponding altitudes, below the $CO_2$ condensation temperature. Temperature profiles corresponding to the spectra in Figs. 17(a,b) are given in Figs. 17(c,d). The development of the temperature inversion at northern mid-latitudes and how the temperature profiles change above the seasonal $CO_2$ polar cap are evident.

# 4. Minor Species

### 4.1 Methane

Four bands of methane ($CH_4$) lie within the spectral range of the PFS, at 1300, 3000, 4400 and 6000 $cm^{-1}$ (Formisano et al., 2004). The 6000 $cm^{-1}$ band is not suitable for detecting weak $CH_4$ signatures by the PFS owing to the presence of many strong solar Fraunhofer lines and the unavailability of the solar spectrum in this region that could be accurately removed from the measurements. In the 4400 $cm^{-1}$ and 1300 $cm^{-1}$ regions, there is some evidence of spectral signatures of minor species. However, the SNR of the PFS is much greater in the 3000 $cm^{-1}$ region; the search for methane was thus made in this band, at 3018 $cm^{-1}$. In order to increase the SNR, 100–200 high-intensity spectra from several orbits were averaged. The resulting global average contains information from 1680 spectra. The continuum is computed by smoothing the spectrum itself over 31 $cm^{-1}$ range. The continuum is then subtracted from the global spectra to obtain a differential spectrum.

Figure 18 shows the calibrated PFS differential spectrum in the 3000 $cm^{-1}$ region averaged over 1680 spectra in the manner described above. A number of solar and water vapour lines can be identified in the spectrum (indicated by S and W). Some

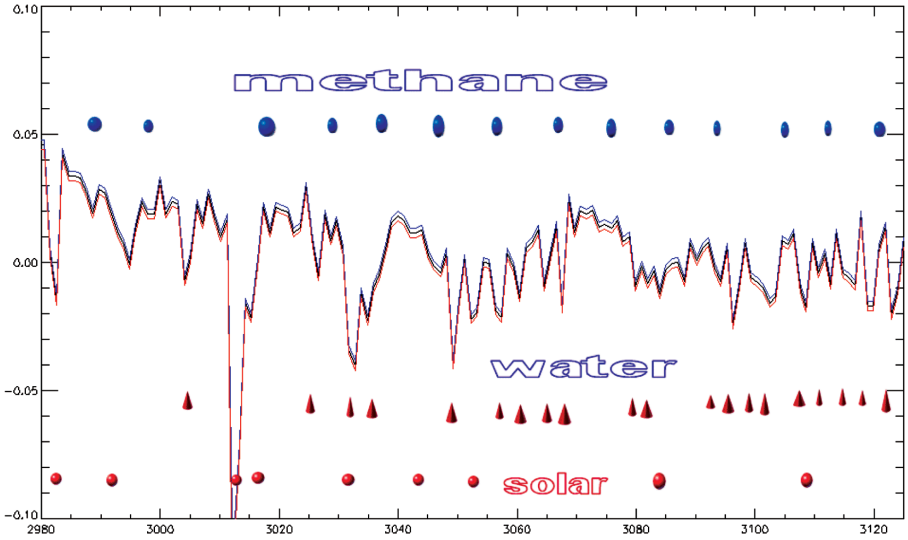


**Fig. 18. PFS differential spectrum (averaged over 1680 measurements) in the region of methane absorption lines. Solar, water and methane line positions are indicated. The three lines shown are the average plus and minus the NER for this average.**

lines are still not identified, as they may be due to other molecules. However, the line at 3018 $cm^{-1}$ is neither solar nor due to water lines; it corresponds to the line position of maximum methane absorption in this wavenumber region. In order to give an error bar on the measured radiance variations, the same spectrum plus or minus a sigma value was also plotted. Sigma was computed from measurements looking at deep space, which in the PFS SW channel corresponds to a zero-level source, and therefore gives a measurement of the instrumental noise. Averaging over 1680 measurements increases the SNR by a factor 40 at least. Figure 18 shows the presence of other possible methane-related features, at 3105, 3075, 3047, 3027 and 2997 $cm^{-1}$. The last three features, however, are also contaminated by water lines and possibly by other molecules.

The line depth at 3018 $cm^{-1}$ can be converted to the actual methane abundance by comparing it to a synthetic spectrum, as discussed below. Figure 19 shows synthetic spectra computed for the assumed martian conditions (6 mb of $CO_2$ atmosphere, 350 ppm or ~30 pr-μm of $H_2O$ at the surface) but with the temperature profile retrieved from the 15 μm band of the same averaged data, and using a solar spectrum constructed for the PFS on the basis of observations and theoretical models (Fiorenza & Formisano, 2005). The general slope of the spectrum is indicative of the presence of water-ice clouds in the equatorial region of Mars. Indeed, the quality of the fits improves noticeably when such clouds are included in the synthetic spectra. In the synthetic spectra, the water-ice clouds have an effective size of 1.25 μm (Clancy et al., 2003), and optical constants from Warren (1984) were used. A deep solar line is present at 3012 $cm^{-1}$, as in the data. The peak on the left-hand side of this line, indicated in Fig. 19 as 'OV' (overshoot), is a characteristic of the PFS monochromatic transfer function (of the sinc type, see Giuranna et al., 2005b). For very thin and intense lines, the function is slightly asymmetric and generates a small overshoot on the left side of the line. The $CH_4$ line is at 3018 $cm^{-1}$. From the direct comparison between the PFS spectrum and the synthetic models (Fig. 19), the observed line depth corresponds to approximately 10 ppb of methane. Considering the statistical uncertainty in the retrieval, the sigma error bar of Fig. 18 and the calibration uncertainty (the transformation of digital units into c.g.s. units brings an increase in the error bar), a conservative $CH_4$ mixing ratio of 10 ± 5 ppb is derived. The synthetic calculations also show that, as the individual lines are not saturated, the depth of the $\nu_3$ Q-branch should increase almost linearly with increasing mixing ratio, and this fact can be used to identify and study variations of the methane mixing ratio.

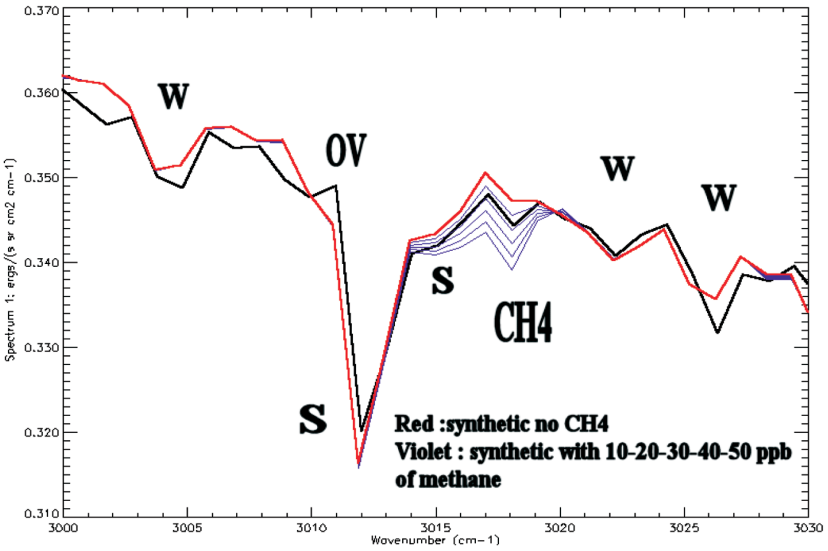


**Fig. 19. PFS average spectrum (black line) with a synthetic spectrum (red) with no methane, and synthetic spectra (blue) with 10, 20, 30, 40 and 50 ppbv of methane.**

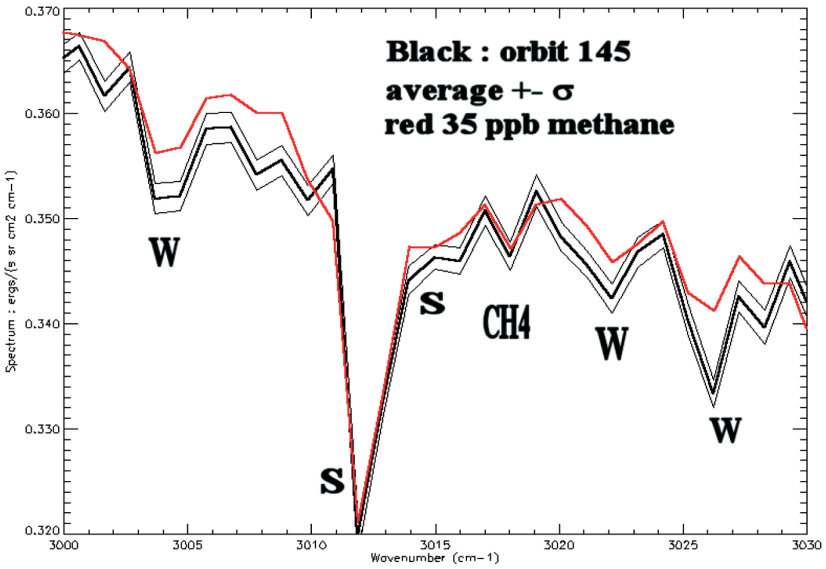


**Fig. 20. PFS average spectrum measured over 120 spectra on orbit 145. The ±NER lines are also shown. The red line is a synthetic spectrum with 35 ppbv of methane.**

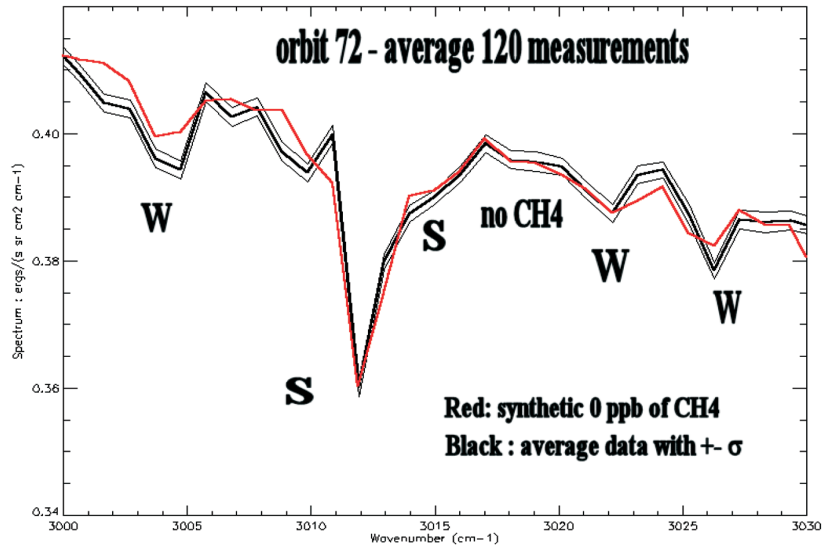


**Fig. 21. PFS average spectrum measured over 120 spectra on orbit 72. The ±NER lines are also shown. The red line is a synthetic spectrum with 0 ppbv of methane.**

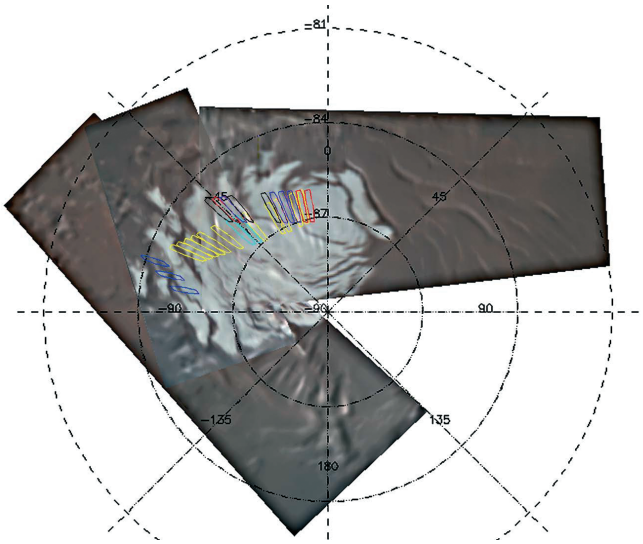


**Fig. 22. Footprints of the PFS observations considered here, inserted into the OMEGA polar cap image. The different colours identify measurements averaged together in the study; data from three different orbits were considered.**

An examination of orbits with higher airmass factor can provide greater confidence in the analysis, as the methane line depth should increase with increasing $CH_4$ amounts along the line-of-sight. This is possible since Mars Express occasionally does not point to the nadir (its normal operation mode), but at a slant angle. This results in an increased air mass in the line-of-sight, which implies that the line-of-sight abundance of methane should also increase, while its mixing ratio is expected to remain unchanged. Figure 20 shows the average over 121 measurements taken during the pericentre pass of orbit 145, with an airmass factor of 1.12. In the figure, the black curve is the measured PFS spectrum with the ±σ thin lines, while the red line provides synthetic spectrum for 35 ppb of methane, but taking into account the airmass factor we obtain 30±5 ppb for the mixing ratio. The value obtained is higher than the global average value of 10 ppb, indicating that the methane mixing ratio may be variable. Motivated by this possibility, several other orbits were examined, including 68, 202 and 72, for which the airmass factors are, respectively, 1.03, 1.33 and 2.1. It was discovered that orbit 72, for which the airmass factor (2.1) was even greater than on orbit 145 (1.12), gives another extreme in $CH_4$. Since the number of measurements for this case (120) is close to those in orbit 145, a similar sigma value is obtained. Figure 21 gives the average PFS spectrum for orbit 72. The uncertainty for this average is shown as ±σ lines. The spectrum is just like the others, with the water lines and the solar lines (together with overshooting) well evident and fitted. However, there is no indication of the methane line, and the synthetic spectrum with no $CH_4$ fits the data nicely. As the synthetic spectrum fitting orbit 72 data was computed using the same solar spectrum as for the previous figures, it is also automatically demonstrated that the 3018 $cm^{-1}$ line in the previous figures was not due to the Sun. From the four orbits 68, 145, 202 and 72, with respective airmass factors of 1.03, 1.12, 1.33 and 2.1, $CH_4$ mixing ratios of 9, 30, 30 and 0 ppb are derived by comparing the observed methane line depth to synthetic spectra, after taking into account the airmass factors. In the case of orbit 72, it is concluded that the $CH_4$ abundance is below the PFS detectability limit, i.e. lower than 5 ppb. The maximum value of methane is three times the global average value given above. Such behaviour seems to indicate $CH_4$ variability over the planet.

### 4.2 HF and HCl

Two other minor species, HF and HBr, have been identified tentatively. Both gases have a number of lines present in the PFS spectrum; some lines are clearly identified, while others may be masked by water or solar lines. For both gases, a number of lines

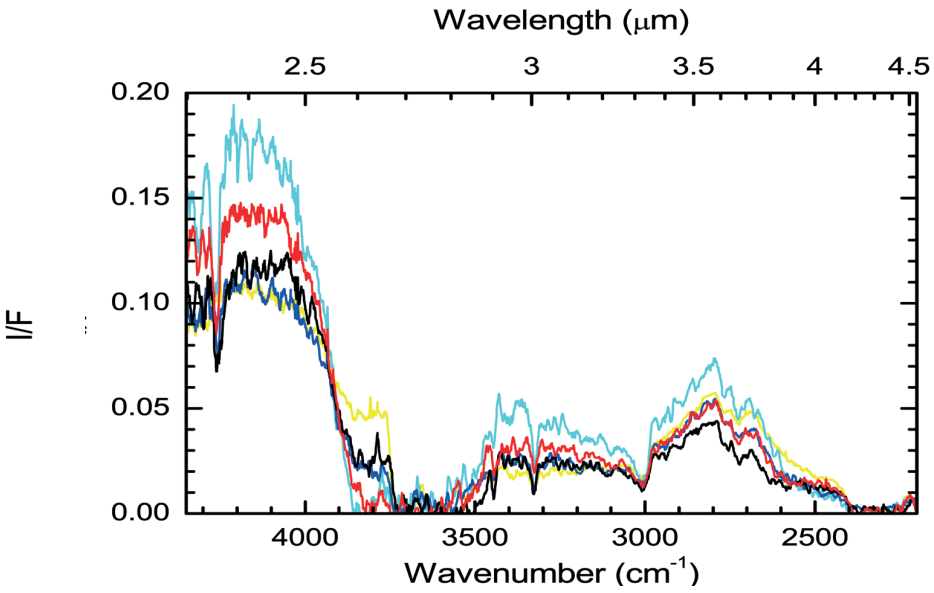


**Fig. 23. The PFS measured spectra over the southern residual polar cap. Colours are the same as in Fig. 22. Only the wavenumbers from 2000 cm$^{-1}$ to 4350 cm$^{-1}$ are shown.**

Table 1. Parameters for $CO_2$ frost models that fit specified PFS residual south polar cap averages shown in Fig. 25.

| *Spectra description* | *$CO_2$ grain radius, mm* | *Mixed water, wt.%* | *Mixed dust, wt.%* | *Frost model scaling* | *Soil spatial fraction* | *Dark neutral spatial I/F* |
|---|---|---|---|---|---|---|
| Orbit 30 average (Fig. 26) | 3.5 | 0.001 | 0.01 | 0.50 | 0.30 | 0.004 |
| Orbit 30 bright spot (Fig. 27) | 8.4 | 0.0005 | 0.06 | 1.38 | 0.0 | 0.0 |
| Orbit 41 A | 7.0 | 0.0007 | 0.05 | 0.77 | 0.095 | 0.004 |
| Orbit 41 B | 10.0 | 0.0003 | 0.03 | 0.77 | 0.09 | 0.0 |
| Orbit 41 C | 10.0 | 0.0005 | 0.05 | 1.00 | 0.05 | 0.0 |
| Orbit 30 avg. BDR | 5.0 | 0.005 | 0.02 | 0.76 | 0.30 | 0.003 |

have been seen, identified and studied. HF is identified clearly at 4075 cm$^{-1}$, while HBr is identified from the 2470 cm$^{-1}$ line. The significance of these findings is still to be established, but the mixing ratios are of the order 200 ppbv for HF and 150 ppbv for HBr. They can certainly contribute to acidic brine, and in general to the acidic conditions of the martian environment.

## 5. South Pole Ice Composition

PFS has also provided important, clear measurements over the polar cap ices, allowing the study of their compositions in terms of water versus carbon dioxide. Modelling of the measured spectra allow us to study the grain sizes of both ices, the percentage of dust present (the model assumes intimate mixing), the presence or absence of soil in the footprint (PFS has a footprint size of 10 km or more, and the presence of soil with no ice must be included). The following shows how some measured spectra were fitted, and the parameters used to obtain the fit.

Five spectral averages were made of the radiance factor ($I/F$) of the residual south cap plus one of an adjoining region with the spectral features of fine-grained water snow, the measurements being taken from three orbits passing over the perennial south polar cap (Hansen et al., 2005). The locations of the spectra used in these averages are depicted in Fig. 22. The average spectra from the different regions are shown in colour in Fig. 23. The average of 11 spectra from orbit 30 (yellow outlines

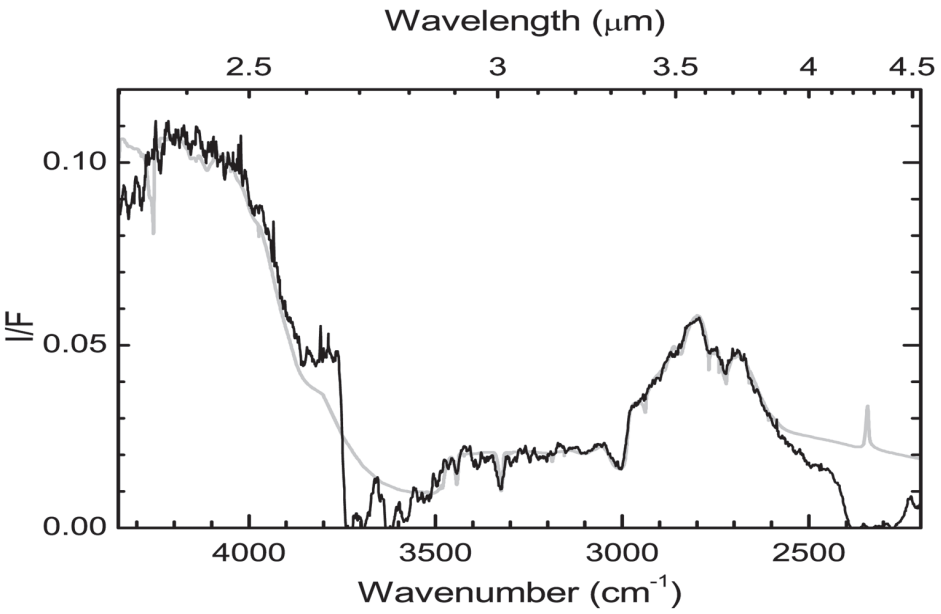


**Fig. 24. The large average for orbit 30 (black line) is shown along with a scaled albedo model fit (grey line). The average is from the 11 yellow footprints shown in Fig. 22; the model parameters are specified in Table 1.**

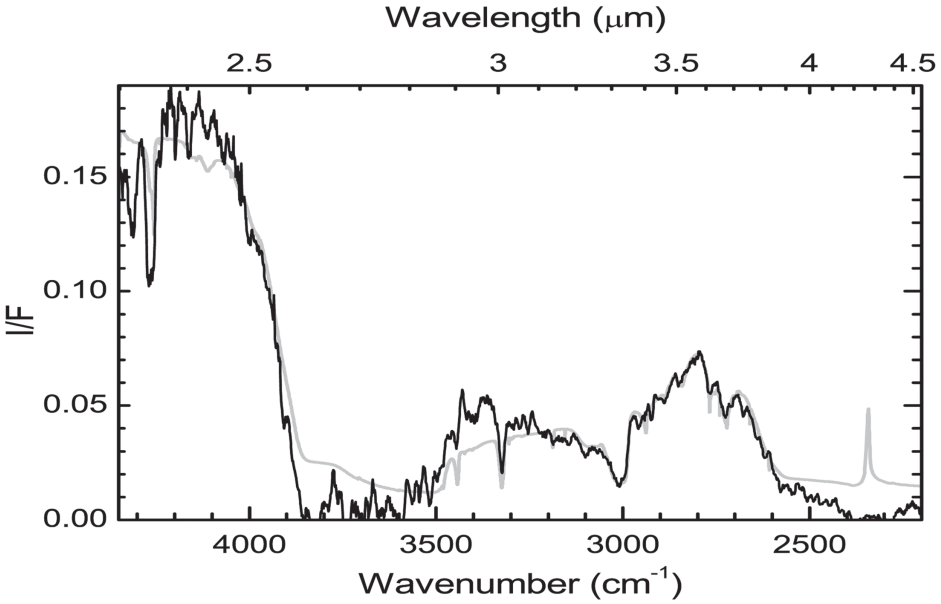


**Fig. 25. The bright average for orbit 30 (black line) is shown along with a scaled albedo model fit (grey line). The average is from the two cyan footprints shown in Fig. 22; the model parameters are specified in Table 1.**

on Fig. 22) is shown in Fig. 24, along with a scaled albedo model. The scaling given in Table 1 is relative to the albedo times the cosine of the incidence angle (~0.18 in this instance), so the numbers are closer to relative abundances and have the same relative units as the soil spectra. There are inaccuracies and uncertainties that cause the sum of the parts in Table 1 to differ from 1.0, such as surface roughness and surface photometry, which are known to be significant factors at large incidence angles. The fit is very good to this low-noise average, at least up to 4300 $cm^{-1}$, except in the regions where the solid $CO_2$ absorption edge is outside the atmospheric absorption bands near 2500 $cm^{-1}$ and 3800 $cm^{-1}$. Here, the level of reflectance is near zero for pure $CO_2$ ice, and is elevated by the intimately and spatially mixed impurities (mainly dust). The exact level and shape of the spectra in these regions are determined by the dust optical constants. In this spectral region, those for terrestrial palagonite are used, although it is not an exact analogue for martian dust. This large average requires about 40% of the area to consist of soil with a spectrum similar to that beyond the polar cap.

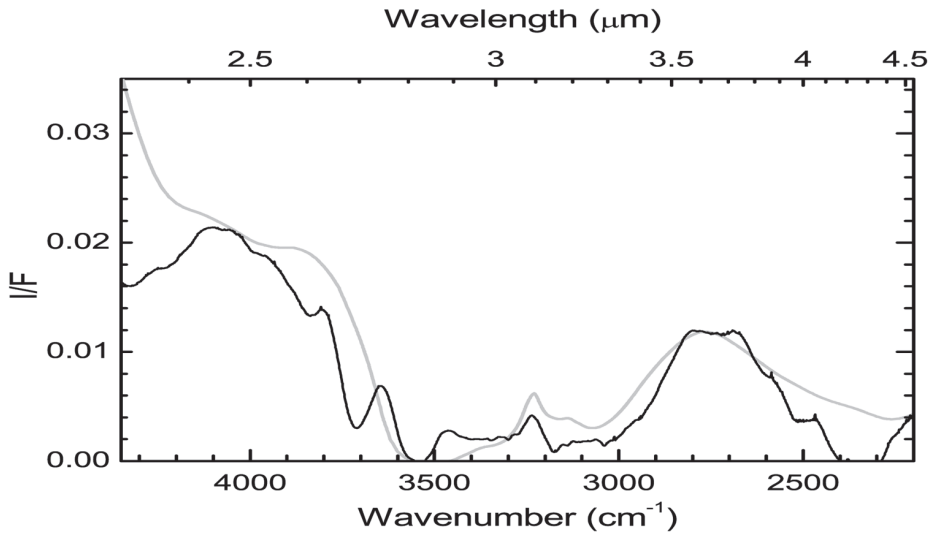


**Fig. 26. Water-ice spectrum at the edge of the residual polar cap. This average is from the areas indicated by the three green outlines in Fig. 22. The scaled BDR model is shown in grey. It is a linear combination of large- and small-grained ice that mimics the height of the reflecting regions around 4000 $cm^{-1}$ and 2750 $cm^{-1}$, and the relative height of the Fresnel reflection peak near 3220 $cm^{-1}$. The mixture consists of about 50% 3 μm and 50% 50 μm snow.**

The average of two especially bright spectra from orbit 30 (cyan outlines in Fig. 22) is shown in Fig. 25. Here, the model fit is optimised to fit the spectrum at wavenumbers below ~3200 $cm^{-1}$, because this is the region that has been calibrated using a black-body radiator. It was not possible to fit the data at wavenumbers >3300 $cm^{-1}$ without significantly losing the fit <3300 $cm^{-1}$. This kind of misfit is common when averaging only two or three spectra, and perhaps would be improved with more spectra to average. This example is larger grained and requires no soil spatial fraction, implying 100% frost coverage in these areas. It is also 30% brighter than a Lambertian plane of frost. This is partly explained by the typical increase in albedo of bright materials at high incidence angles, and partly by non-Lambertian behaviour of the frost scattering.

Three sets of spectra were selected from the available orbit 41 data, based on their similarity across the spectral range investigated here. The first average consisting of four spectra (blue in Fig. 22) is similar to the large average of orbit 30. The second average of three spectra (black in Fig. 22) is slightly brighter at large wavenumbers and darker at small wavenumbers than the first average. The final average consisting of three spectra (red in Fig. 22) is similar to the bright average of orbit 30. Not shown, for brevity, are the figures of these data and their fit (Hansen et al., 2005). In all three cases, for the same reason as before, the fit was held tightly below 3200 $cm^{-1}$, with some misfit at larger wavenumbers appearing in averages two and three. The fits are generally better in the first two than in any of the others from either orbit. The model grain sizes are slightly larger than those from orbit 30, and all present FOVs more filled by frost (≤10% soil area) than the large orbit 30 average.

To investigate the sensitivity of the models to the lighting geometry, bi-directional reflectance (BDR) models were run to compare with the scaled albedo models. The BDR spectrum looks more like the normal albedo spectrum but with a factor 2–5 less dust and water ice. The normal albedo with the same impurity amounts as the high-incidence models is too dark in the 2800–3500 $cm^{-1}$ region, and the albedo model at 79° incidence looks even purer than the BDR. A BDR model (multiplied by π) is described in Table 1 as adjusted to fit the orbit 30 large average, with a fit comparable to the scaled normal albedo model. The implication is that the measured spectra are consistent with 2–5 times the dust and water than in the albedo models described in Table 1.

On orbit 61, a region at the edge of the south polar residual cap was found that looked very much like a fine-grained water frost. Figure 26 shows the average of three spectra (indicated by the green outlines in Fig. 22), smoothed over wavenumber

because there are no fine-resolution features in the spectrum of water snow. Also shown in Fig. 26 is a model that fits it. The model is based on a bi-directional reflectance model of water snow at ~150K at the lighting geometry consistent with the observation. The model is adjusted to fit the peak reflection at 2800 $cm^{-1}$ and 4000 $cm^{-1}$, and the height of the Fresnel reflectance peak of water-ice at 3220 $cm^{-1}$. The model consists of a spatial mixture of fine-grained water ice (to match the high reflectance) and large-grained water ice (to match the Fresnel peak). The relative abundances of fine-grained ($r = 3$ μm) snow and coarse-grained ($r \geq 50$ μm) snow are about equal and the model is scaled by a factor of about 0.8 (implying a small amount of shadow in the footprints).

The model simulation of the PFS south polar cap spectra shows that the principal component of ice is, of course, solid carbon dioxide. However, best fits require some admixture, with water-ice amounting to (allowing for uncertainties owing to lighting geometry) not more than several tens of ppm by mass. The effective grain sizes are typically 5–10 mm, and the dust content is a few times $10^{-4}$. These results are very similar to those from telescopic measurements of the mid-summer south polar cap in the same wavelength region (Glenar et al., 2005). A very different estimate of 15% for the $H_2O/CO_2$ mixing ratio was published by Bibring et al. (2004), on the basis of spectra obtained by OMEGA in the 2–2.6 μm wavelength range. It seems the discrepancy is related to the models rather than the data. The team's assumption is that the $CO_2$ and $H_2O$ are sufficiently different in volatility that they condense discretely and mix heterogeneously, like dust and ice. It is assumed that the water is mostly from atmospheric condensation and has grain sizes typical of atmospheric water-ice particles. The Bibring et al. (2004) model, on the other hand, assumes a molecular mixture of $CO_2$ and $H_2O$, which would be expected to produce different results to the grain mixture. The spots of high water-ice abundance in the OMEGA data, however, correspond well with the water-ice regions sampled by PFS on orbit 61 (Fig. 26). Finally, it should be stressed that only information about the composition of a thin layer can be derived from the IR spectra. What is below cannot be studied with IR remote-sensing techniques. But a predominantly $CO_2$-covered residual south polar cap at a time when it is at its smallest extent (at the end of summer) proves from a spectroscopic point of view what thermal measurements have shown before: the persistence of $CO_2$ is the normal state of affairs for the south over at least the last 30 years, even in the face of rapidly changing small-scale terrain features (Malin et al., 2001).

## 6. Signatures of the Solar Spectrum

The intensities of 10 solar lines relative to the continuum, which is given in Table 1 in PFS units [erg/(s sr $cm^2$ $cm^{-1}$)], have been studied. The intensity of a solar line relative to the continuum should remain constant in time if the line is not variable (as assumed) and if there are no systematic errors in the measurements. The lines considered (Table 2) range from wavenumber 2468 $cm^{-1}$ to 3012 $cm^{-1}$. Their intensities with respect to the continuum span from 2.1% to 8.5%. Although there is a systematic difference in the continuum owing to higher soil temperature for PFS, the solar line intensities are essentially identical for PFS and ISO; indeed, the deviation on average seems to be only 0.02%. lt appears clear that the overshoot is present in the PFS data only for the most intense lines. If the average error on the line intensities is considered as due to noise, then there is an SNR of the order 3000 in the wavenumber range considered here (for this average of 1680 PFS measurements).

The last column in Table 2 gives the FWHM of the lines studied. This quantity is useful for checking the spectral resolution of PFS; on average, the FWHM is of the order 1.5 $cm^{-1}$. This does not disagree with the quoted spectral resolution of 1.3 cm resulting from studies of synthetic spectra fitting PFS measurements, because single solar lines were not necessarily selected. It may well be that some of the lines are multiple solar lines, in which case the FWHM would not be expected to be representative of the PFS spectral resolution.

Table 2. The intensities of solar lines.

| *ISO data* | | | *PFS data* | | | | |
|---|---|---|---|---|---|---|---|
| *Line cm$^{-1}$* | *continuum* | *%* | *continuum* | *%* | *Overshoot* | *Differences* | *FWHM cm$^{-1}$* |
| 2468 | 0.440 | 4.9 | 0.735 | 4.2 | no | 0.7 | 1.7 |
| 2557 | 0.436 | 2.5 | 0.667 | 2.4 | no | 0.1 | 2.0 |
| 2587 | 0.430 | 6.5 | 0.641 | 7.1 | yes | –0.6 | 1.3 |
| 2669 | 0.428 | 2.1 | 0.597 | 1.8 | no | 0.3 | 1.8 |
| 2673 | 0.425 | 2.8 | 0.592 | 2.0 | no | 0.8 | 1.7 |
| 2704 | 0.421 | 3.1 | 0.574 | 3.3 | no | –0.2 | 1.3 |
| 2716 | 0.418 | 3.1 | 0.566 | 4.0 | yes | –0.9 | 1.0 |
| 2719 | 0.416 | 3.1 | 0.563 | 3.0 | no | 0.1 | 1.8 |
| 2747 | 0.404 | 2.2 | 0.537 | 2.4 | yes | –0.2 | 1.2 |
| 3012 | 0.270 | 8.5 | 0.355 | 8.4 | yes | 0.1 | 1.6 |
| | | | | | average | 0.02 | |

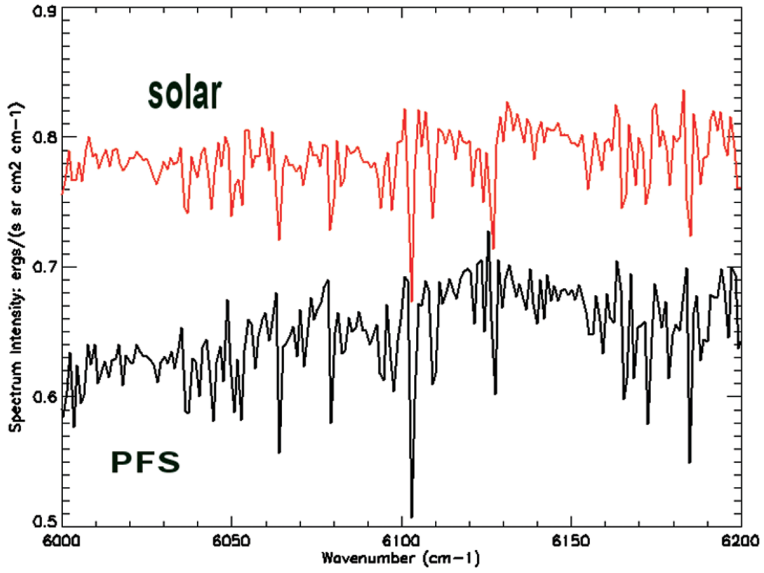


**Fig. 27. The PFS spectrum compared with the assembled solar spectrum: almost all the lines observed in this region are of solar origin.**

Finally, a comparison was made of a measured PFS spectrum in the range 6000–6200 cm$^{-1}$ with the solar spectrum assembled by Fiorenza & Formisano (2005) for PFS. The results are shown in Fig. 27. Essentially, all the observed lines in this range appear to be solar in origin. It is important to note that the solar spectrum in this region has many major lines and has never before been measured from space. In Earth-based observations, the saturated water bands in the atmosphere prevent the study of the solar lines in this wavenumber range. There are 41 solar lines identified in this portion of the spectrum that are also observed by PFS. Only six lines in the PFS spectrum do not correspond to solar lines, and three minor solar lines are not seen by PFS, possibly because of insufficient spectral resolution. The relative intensities of the measured lines correspond very well to the intensity of the assembled solar spectrum.

## 7. Conclusions

The first PFS results have been reviewed here. PFS has worked well and produced interesting results for the range of wavenumbers explored. A comparison with the ISO SWS spectrum has been performed and has demonstrated good measurements to the lower radiance intensity level (fraction of the 0.1% level in the 1680-measurement average spectrum). The atmosphere is well studied by the LW channel; the SW channel adds minor-species composition, soil features and non-LTE emission. Finally, the details of the solar spectrum seem to appear clearly in the PFS spectrum, measured from space for the first time.

## Acknowledgements

The PFS experiment was built at the Istituto di Fisica dello Spazio Interplanetario (IFSI) of the Istituto Nazionale di Astrofisica (INAF), and was funded by ASI in the context of the Italian participation in the Mars Express mission of ESA.

## References

Bibring, J.-P., Langevin, Y., Poulet, F., Gendrin, A., Gondet, B., Berthe, M., Soufflot, A., Drossart, P., Combes, M., Bellucci, G., Maroz, V., Mangold, N. & Schmitt, B. (2004). Perennial water ice identified in the south polar cap of Mars. *Nature* **428**, 6983–6986.

Clancy, R.T., Lee, S.W., Gladstone, G.R., McMillan, W.W. & Rousch, T. (1995). A new model for Mars atmospheric dust based upon analysis of ultraviolet through infrared observations from Mariner 9, Viking, and PHOBOS. *J. Geophys. Res.* **100**(E3), 5251–5263.

Clancy, R.T., Wolff, M.J. & Christensen, P.R. (2003). Mars aerosol studies with the MGS TES emission phase function observations: optical depths, particle sizes, and ice cloud types versus latitude and solar longitude. *J. Geophys. Res.* **100**(E9), 2–1, CiteID 5098, DOI: 10.1029/2003JE002058.

Conrath, B.J. (1975). Thermal structure of the martian atmosphere during the dissipation of the dust storm of 1971. *Icarus* **24**, 36–46.

Fedorova, A.A., Leilouch, E., Titov, D.V., de Graauw, T. & Feuchtgruber, H. (2002). Remote sounding of the martian dust from ISO spectroscopy in the 2.7 μm bands. *Planet. Space Sci.* **50**(1), 3–9.

Fiorenza, C. & Formisano, V. (2005). A solar spectrum for PFS data analysis. *Planet. Space Sci.*; in Press.

Forget, F., Hourdin, F., Fournier, R., Hourdin, C., Talagrand, O., Collins, M., Lewis, S.R., Read, P.L. & Huot, J. (1999). Improved general circulation models of the martian atmosphere from the surface to above 80 km. *J. Geophys. Res.* **100**(E10), 24155–24176.

Formisano, V., Angrilli, F., Amold, G., Atreya, S., Bianchini, G., Biondi, D., Blanco, A., Blecka, M.I., Coradini, A., Colangeli, L., Ekonomov, A., Encrenaz, T., Esposito, F., Fonti, S., Giuranna, M., Grassi, D., Gnedykh, V., Grigoriev, A., Hansen, G., Hirsh, H., Khatuntsev, I., Kiselev, A., Ignatiev, N., Jurewicz, A., Lellouch, E., Lopez Moreno, J., Marten, A., Mattana, A., Maturilli, A., Mencarelli, E., Michalska, M., Moroz, V., Moshkin, B., Nespoli, F., Nikolsky, Y., Orfei, R., Orleanski, P., Orofino, V., Palomba, E., Patsaev, D., Piccioni, G., Rataj, M., Rodrigo, R., Rodriguez, J., Rossi, M., Saggin, B., Titov, D. & Zasova, L. (2005a). The Planetary Fourier Spectrometer (PFS) onboard the European Mars Express mission. *Planet. Space Sci.* **53**, 963–974.

Formisano, V., Atreya, S., Encrenaz, T., Ignatiev, N. & Giuranna, M. (2004). Detection of methane in the atmosphere of Mars. *Science* **306**, 1758.

Formisano, V., Encrenaz, T., Fonti, S., Giuranna, M., Grassi, D., Hirsh, H., Khatuntsev, I., Ignatiev, N., Lellouch, E., Maturilli, A., Moroz, M., Orleanski, P., Piccioni, G., Rataj, M., Saggin, B. & Zasova, L. (2005b). A martian PFS average spectrum: Comparison with ISO SWS. *Planet. Space Sci.* **53**, 1043–1052.

Formisano, V., Maturilli, A., Giuranna, M., D'Aversa, E. & Lopez-Valverde, M.A. (2005c). PFS-MEX observations of non-LTE emission at 4–5 μm. *Icarus* (submitted).

Giuranna, M, Formisano, V., Biondi, D., Ekonomov, A., Fonti, S., Grassi, D., Flirsch, H., Khatuntsev, I., Ignatiev, N., Michalska, M., Mattana, A., Maturilli, A., Mencarelli, E., Nespoli, F., Orfei, R., Orleanski, P., Piccioni, G., Rataj, M., Saggin, B. & Zasova, L.

(2005a). Calibration of the Planetary Fourier Spectrometer Long Wavelength Channel. *Planet. Space Sci.* **53**, 993–1007.

Giuranna, M, Formisano, V., Biondi, D., Ekonomov, A., Fonti, S., Grassi, D., Hirsch, H., Khatuntsev, I., Ignatiev, N., Michalska, M., Mattana, A., Maturilli, A., Mencarelli, E., Nespoli, F., Orfei, R., Orleanski, P., Piccioni, G., Rataj, M., Saggin, B. & Zasova, L. (2005b). Calibration of the Planetary Fourier Spectrometer Short Wavelength Channel. *Planet. Space Sci.* **53**, 975–991.

Glenar, D.A., Hansen, G., Bjoraker, G., Smith, M., Pearl, J. & Blaney, D. (2005). Bright-region radiative properties within the Mars south polar cap ($L_s$=231) from near-infrared spectroscopic imaging. *Icarus*; in Press.

Grassi, D., Ignatiev, N.I., Zasova, L.V., Maturilli, A., Formisano, V., Bianchini, G.A. & Giuranna, M. (2005a). Methods for the analysis of data from the Planetary Fourier Spectrometer on board of the Mars Express mission. *Planet. Space Sci.* **53**, 1017–1034.

Grassi, D., Fiorenza, C., Zasova, L.V., Ignatiev, N.I., Maturilli, A., Formisano, V. & Giuranna, M. (2005b). The martian atmosphere above great volcanoes: Early Planetary Fourier Spectrometer observations. *Planet. Space Sci.* **53**, 1053–1064.

Hansen, G., Giuranna, M., Formisano, V., Fonti, S., Grassi, D., Hirsh, H., Ignatiev, N., Maturilli, A., Orleanski, P., Piccioni, G., Rataj, M., Saggin, B. & Zasova, L. (2005). PFS-MEX observations of ices in the residual south polar caps of Mars. *Planet. Space Sci.* **53**, 1089–1095.

Ignatiev, N.I., Grassi, D. & Zasova, L.V. (2005). Planetary Fourier Spectrometer data analysis: fast radiative transfer models. *Planet. Space Sci.* **53**, 1035–1042.

Lellouch, E., Encrenaz, T., de Graauw, T., Erard, S., Morris, P., Crovisier, J., Feuchtgruber, H., Girard, T. & Burgdorf, M. (2000). The 2.4–45 μm spectrum of Mars observed with the Infrared Space Observatory. *Planet. Space Sci.* **48**, 1393.

Lopez-Valverde, M.A., Lopez Puertas, M., Lopez Moreno, J.J., Formisano, V., Grassi, D., Maturilli, A., Lellouch, E. & Drossart, P. (2005). Simulation of non-LTE $CO_2$ emissions at 4.3 μm in the martian atmosphere as observed by PFS/ Mars Express and SWS/ISO. *Planet. Space Sci.* **53**, 1079–1087.

Malin, M.C., Caplinger, M.A. & Davis, S.D. (2001). Observational evidence for an active surface reservoir of solid carbon dioxide on Mars. *Science* **294**, 2146–2148.

Mellon, M. (2002). TES thermal inertia global map. NASA Planetary Data System, GLOBAL_TI_60N_50S_8PPD.

Smith, D.E., Neumann, G., Arvidson, R.E., Guinness, E.A. & Slavney, S. (2003). Mars Global Surveyor laser altimeter mission experiment gridded data record. NASA Planetary Data System, MGS-M-MOLA-5-MEGDR-L3-V1.0.

Smith, M.D., Pearl, J.C., Conrath, B.J. & Christensen, P.R. (2000). Mars Global Surveyor Thermal Emission Spectrometer (TES) observations of dust opacity during aerobraking and science phasing. *J. Geophys. Res.* **105**(E4), 9539–9552.

Titov, D.V., Fedorova, A.A. & Haus, R. (2000) A new method of remote sounding of the martian aerosols by means of spectroscopy in the 2.7 μm band. *Planet. Space Sci.* **48**(1), 67–74.

Warren, S.G. (1984). Optical constants of ice from the ultraviolet to the microwave. *Applied Optics* **23**, 1206–1225.

Zasova, L., Formisano, V., Moroz, V., Grassi, D., Ignatiev, N., Giuranna, M., Hansen, G., Blecka, M., Ekonomov, A., Lellouch, E., Fonti, S., Grigoriev, A., Hirsch, H., Khatuntsev, I., Mattana, A., Maturilli, A., Moshkin, B., Patsaev, D., Piccioni, G., Rataj, M. & Saggin, B. (2005). Water clouds and dust aerosols observations with PFS MEX at Mars. *Planet. Space Sci.* **53**, 1065–1077.

Zurek, R.W., Barnes, J.R., Haberle, R.M., Pollack, J.B., Tillman, J.E. & Leovy, C.B. (1992). Dynamics of the atmosphere of Mars. In *Mars* (Eds. H.H. Kieffer, B.M. Jakowsky, C.W. Snyder & M.S. Matthews), The University of Arizona Press., Tucson, USA, pp835–933.